EDGE ARTICLE

Check for updates

From $H_{12}C_4N_2CdI_4$ to $H_{11}C_4N_2CdI_3$: a highly polarizable $CdNI_3$ tetrahedron induced a sharp enhancement of second harmonic generation response and birefringence†

Huai-Yu Wu,[a] Chun-Li Hu,*[b] Miao-Bin Xu,[a] Qian-Qian Chen,[b] Nan Ma,[b] Xiao-Ying Huang, [ID] [b] Ke-Zhao Du [ID] *[a] and Jin Chen [ID] *[ab]

In this study, we identify a novel class of second-order nonlinear optical (NLO) crystals, non-π-conjugated piperazine ($H_{10}C_4N_2$, PIP) metal halides, represented by two centimeter-sized, noncentrosymmetric organic–inorganic metal halides (OIMHs), namely $H_{12}C_4N_2CdI_4$ ($P2_12_12_1$) and $H_{11}C_4N_2CdI_3$ (Cc). $H_{12}C_4N_2CdI_4$ is the first to be prepared, and its structure contains a CdI_4 tetrahedron, which led to a poor NLO performance, including a weak and non-phase-matchable second harmonic generation (SHG) response of $0.5 \times KH_2PO_4$ (KDP), a small birefringence of 0.047 @1064 nm and a narrow bandgap of 3.86 eV. Moreover, $H_{12}C_4N_2CdI_4$ is regarded as the model compound, and we further obtain $H_{11}C_4N_2CdI_3$ via the replacement of CdI_4 with a highly polarizable $CdNI_3$ tetrahedron, which results in a sharp enhancement of SHG response and birefringence. $H_{11}C_4N_2CdI_3$ exhibits a promising NLO performance including $6 \times KDP$, 4.10 eV, $\Delta n = 0.074$ @1064 nm and phase matchability, indicating that it is the first OIMH to simultaneously exhibit strong SHG response ($>5 \times KDP$) and a wide bandgap (>4.0 eV). Our work presents a novel direction for designing high-performance NLO crystals based on organic–inorganic halides and provides important insights into the role of the hybridized tetrahedron in enhancing the SHG response and birefringence.

Introduction

Nonlinear optical (NLO) materials, particularly second harmonic generation (SHG) crystals, offer effective ways for tuning the laser wavelength and expanding its spectral range.[1–6] Traditionally, high-quality second-order NLO crystals must satisfy several fundamental conditions, such as exhibiting a noncentrosymmetric structure, possessing a strong SHG effect, having a wide bandgap and transmission window, featuring appropriate birefringence for phase matchability, and having a conducive crystal growth method.[7–10] To date, several commercialized NLO crystals have been used, including $KBe_2BO_3F_2$ (KBBF), β-BaB_2O_4 (BBO), KH_2PO_4 (KDP), $KTiOPO_4$ (KTP), $AgGaS_2$ (AGS), and α-$LiIO_3$.

Over the past few years, interest in the development of semi-organic NLO crystals has been steadily increasing. These crystals feature many advantages such as the availability of a wide range of organic components, tunability of inorganic structures, and ease of single crystal growth.[11–15] Notably, the compounds containing π-conjugated organic moieties have attracted the most attention, and many promising NLO materials in such classes have been reported, such as $KLi(HC_3N_3O_3)\cdot 2H_2O$ (5.3 × KDP),[11] $Lu_5(C_3N_3O_3)(OH)_{12}$ (4.2 × KDP),[12] $C(NH_2)_3SO_3F$ (5 × KDP),[13] $(C_5H_6ON)^+(H_2PO_4)^-$ (3 × KDP),[14] and $[o\text{-}C_5H_4NHOH]_2[I_7O_{18}(OH)]\cdot 3H_2O$ (8.5 × KDP).[15] Alongside these compounds, several organic–inorganic metal halides (OIMHs) formed from the combination of a π-conjugated organic cation with a metal-halide polyhedron have also been discovered to show NLO performance, such as $(H_7C_3N_6)(H_6C_3N_6)MCl_3$ (M = Hg and Zn; 5 × and 2.8 × KDP),[16,17] $[C_{18}H_{21}N_4][AgX_3]X$ (X = Cl, Br, and I, 6.2, 6.5 and 7.6 × KDP),[18] α-$(CN_3H_6)_3Cu_2I_5$ (1.8 × KDP),[19] and $(C_6H_{11}N_2)PbBr_3$ (8 × KDP).[20]

It is also worth studying the NLO properties of non-π-conjugated OIMHs, which is similar to the approach of expanding the chemical system from π-conjugated borates to non-π-conjugated phosphates or sulfates.[21–27] Traditionally, the introduction of metal cations with stereo-chemically active lone-pair electrons (SCALP cation, e.g. Bi^{3+}, Pb^{2+}, and Ge^{2+}) or d^{10} transition metal cations (d^{10}-TM cation, e.g. Zn^{2+} and Cd^{2+}) can effectively design novel SHG-active non-π-conjugated OIMHs.[28–34] However, on the one hand, the use of SCLAP cations

[a]College of Chemistry and Materials Science, Fujian Normal University, Fuzhou, 350002, China. E-mail: cj2015@fjnu.edu.cn

[b]State Key Laboratory of Structural Chemistry, Fujian Institute of Research on the Structure of Matter, Chinese Academy of Sciences, Fuzhou, 350002, P. R. China

is known to cause red shifts in absorption edges and reduce bandgaps of the resulting crystals, limiting their potential applications in the ultraviolet (UV) and deep-UV regions.[35–40] For instance, Mao's group recently reported a series of Ge^{2+}-containing OIMHs, in which $(CH_3NH_3)GeBr_3$ shows a large SHG response (5.3 × KDP) but a small bandgap (2.91 eV). There are also similar cases to $C_4H_9NOBiBr_7$ (2.2 × urea, 2.67 eV) and $(C_6H_5(CH_2)_4NH_3)_4BiI_7 \cdot H_2O$ (1.3 × AGS, 2.29 eV).[41] On the other hand, many non-π-conjugated OIMHs with d^{10}-TM cations, such as $(C_4H_{10}NO)_2Cd_3Cl_6$,[42] $(L/D-C_{10}H_{20}N_2O_4)_2Cd_5Cl_{12}$,[43] $L/D-C_6H_{10}N_3O_2ZnBr_3$,[44] $[C_5H_{14}NO]CdCl_3$,[45] $L/D-C_{12}H_{20}N_6O_4Cd_2Cl_5$,[44] and $((CH_3)_3NCH_2Cl)CdCl_3$,[46] usually possess wide bandgaps (>5.0 eV) but relatively weak SHG effects (<1.0 × KDP). Hence, it is challenging to develop NLO OIMHs that simultaneously exhibit both a strong SHG effect (>5 × KDP) and wide bandgap (>4.0 eV).

To overcome this challenge, our efforts are focused on the non-π-conjugated organic moiety-$Cd^{2+}/Zn^{2+}-I^-$ system. In the beginning, a noncentrosymmetric OIMH, $H_{12}C_4N_2CdI_4$, has been hydrothermally prepared. But our experimental results show that this compound has a small bandgap (3.86 eV) along with a weak and non-phase-matchable SHG response (0.5 × KDP). Such an undesired NLO performance could be attributed to the high symmetry and weak anisotropy of the CdI_4 tetrahedron. To the best of our knowledge, this phenomenon is reminiscent of metal sulfates based on a tetrahedral SO_4^{2-} unit. And in metal sulfates, one effective route to overcome this problem is to partially substitute O atoms in SO_4^{2-}, as seen in $LiSO_3F$,[47] $Na_{10}Cd(NO_3)_4(SO_3S)_4$,[48] $Ba(NH_2SO_3)_2$,[49] $Ba(SO_3CH_3)_2$,[50] and so on. Hence, furthermore, $H_{12}C_4N_2CdI_4$ is regarded as the model compound, and we consider that the coordination of $H_{10}C_4N_2$ with a Cd^{2+} cation could result in the partial substitution of I^- anions in the CdI_4 tetrahedron, forming a polarizable Cd–I–N unit, which could enhance the SHG response and birefringence in new OIMHs. Additionally, we also hope that new compound involves a smaller number of I^- anions in order to exhibit a wider bandgap. Therefore, a novel OIMH, namely $H_{11}C_4N_2CdI_3$, is prepared *via* regulating the synthetic conditions of $H_{12}C_4N_2CdI_4$ (a lower concentration of I^- anions in the reaction system). $H_{11}C_4N_2CdI_3$ contains a distorted $CdNI_3$ tetrahedron and demonstrates superior NLO performance in comparison to $H_{12}C_4N_2CdI_4$. Specifically, $H_{11}C_4N_2CdI_3$ exhibits a strong and phase-matchable SHG effect (6 × KDP), large birefringence ($\Delta n = 0.062$ @1064 nm), and a wide bandgap (4.10 eV), indicating its potential as a promising ultraviolet NLO material.

Methods

Materials and synthesis

CdO (>99%), Y_2O_3 (>99%), and piperazine (>99%), HI (55–58% wt), were used as purchased from Adamas-beta. There are different synthesis conditions of $H_{12}C_4N_3CdI_4$ and $H_{11}C_4N_2CdI_3$ (Table S1†), and the best conditions (larger size and higher yields) are mentioned as follows. For the preparation of $H_{12}C_4N_2CdI_4$, the starting materials are CdO, (256.8 mg, 2 mmol), piperazine (86.14 mg, 1 mmol), HI (2 mL) and H_2O (1

mL). A mixture of the starting materials was placed in Teflon pouches (23 mL) sealed in an autoclave which was heated at 90 °C for 72 hours, and cooled to 30 °C at 1.67 °C h^{-1}. Yellow block-shaped crystals of $H_{12}C_4N_2CdI_4$ were obtained in high yields of ~95% (based on Cd). For the preparation of $H_{11}C_4N_2CdI_3$, the starting materials are CdO, (128.4 mg, 1 mmol), Y_2O_3, (112.5 mg, 0.5 mmol), piperazine (172.28 mg, 2 mmol), HI (1 mL) and H_2O (2 mL). A mixture of the starting materials was placed in Teflon pouches (23 mL) sealed in an autoclave which was heated at 110 °C for 72 hours, and cooled to 30 °C at 1.67 °C h^{-1}. Yellow block-shaped crystals of $H_{11}C_4N_2CdI_3$ were obtained in high yields of ~95% (based on Cd).

Single crystal structure determination

Single-crystal X-ray diffraction data for the title compounds were collected on an Xcalibur, Eos, Gemini diffractometer with Mo Kα radiation ($\lambda = 0.71073$ Å) at 293 K and a Rigaku XtaLAB Synergy-DW dual-wavelength CCD diffractometer with Cu Kα radiation ($\lambda = 1.54184$ Å) at 109 K. Data reduction was performed with CrysAlisPro, and absorption correction based on the multi-scan method was applied.[51] The structures of $H_{12}C_4N_2CdI_4$ and $H_{11}C_4N_2CdI_3$ were determined by the direct methods and refined by full-matrix least-squares fitting on F^2 using SHELXL-2014.[52] All of the non-hydrogen atoms were refined with anisotropic thermal parameters. The structure was checked for missing symmetry elements using PLATON, and none were found.[53] The Flack parameters refined for $H_{12}C_4N_2CdI_4$ and $H_{11}C_4N_2CdI_3$ are 0.45(12) and −0.01(2), respectively, indicating the correctness of their absolute structures. In addition, twinning was observed in $H_{12}C_4N_2CdI_4$ and $H_{11}C_4N_2CdI_3$, and the twin laws of these compounds were (−1.0, 0.0, 0.0, 0.0, −1.0, 0.0, 0.0, 0.0, −1.0) and (−1.0, 0.0, 0.0, 0.0, −1.0, 0.0, 0.0, 0.0, −1.0), respectively. Crystallographic data and structural refinements of the compounds are listed in Tables S2–S6.†

Powder X-ray diffraction

Powder X-ray diffraction (PXRD) patterns were recorded on a Rigaku Ultima IV diffractometer with graphite-monochromated Cu Kα radiation in the 2θ range of 10–70° with a step size of 0.02°.

Thermal analysis

Thermogravimetric analysis (TGA) was performed with a Rigaku TG-DTA 8121 unit under an Ar atmosphere, at a heating rate of 10 °C min^{-1} in the range from 30 to 800 °C.

Optical measurements

The infrared (IR) spectrum was recorded on a Thermo Fisher Nicolet 5700 FT-IR spectrometer in the form of KBr pellets in the range from 4000 to 400 cm^{-1}.

The ultraviolet-visible-infrared (UV-vis-IR) spectrum in the range of 200–800 nm was recorded on a PerkinElmer Lambda 750 UV-vis-NIR spectrophotometer. The reflectance spectrum was converted into an absorption spectrum by using the Kubelka–Munk function.[54]

Second harmonic generation measurements

Powder SHG measurements were carried out with a Q switch Nd:YAG laser generating radiation at 1064 nm according to the method of Kurtz and Perry.[55] Crystalline $H_{12}C_4N_2CdI_4$ and $H_{11}C_4N_2CdI_3$ samples were sieved into distinct particle-size ranges (50–70, 70–100, 100–140, 140–200, 200–250 and 250–325 μm). Sieved KH_2PO_4 (KDP) samples in the same particle-size ranges were used as references.

Elemental analysis

The elemental content was measured on a Vario EL Cube elemental analyzer from Elementar Analysensysteme GmbH, Germany. The combustion temperature was 800 °C (Table S7†).

Energy-dispersive X-ray spectroscopy

Microprobe elemental analyses were performed and the elemental distribution maps were obtained on a field-emission scanning electron microscope (Phenom LE) equipped with an energy-dispersive X-ray spectroscope (EDS, Phenom LE).

Computational method

The electronic structures and optical properties were obtained using a plane-wave pseudopotential method within density functional theory (DFT) implemented in the total energy code CASTEP.[56,57] For the exchange and correlation functional, we chose Perdew–Burke–Ernzerhof (PBE) in the generalized gradient approximation (GGA).[58] The interactions between the ionic cores and the electrons were described by the norm-conserving pseudopotential.[59] The following orbital electrons were treated as valence electrons: I-$5s^25p^5$, Cd-$4s24p^65s^2$, H-$1s^1$, C-$2s^22p^2$ and N-$2s^22p^3$. The numbers of plane waves included in the basis sets were determined at a cutoff energy of 700 eV. During the SCF and optical-property calculations of the two compounds, the k-point separation was set to 0.04 $Å^{-1}$ to perform the numerical integration of the Brillouin zone, and the corresponding k-point samplings are $3 \times 2 \times 2$ and $2 \times 4 \times 2$ for $H_{12}C_4N_2CdI_4$ and $H_{11}C_4N_2CdI_3$, respectively. After the principal axis transformation, the k-point sampling of $H_{11}C_4N_2CdI_3$ changes to $2 \times 3 \times 2$ when the k-point separation is 0.04 $Å^{-1}$. The other parameters and convergent criteria were the default values of the CASTEP code.[56,57]

The calculations of second-order NLO susceptibilities were based on length-gauge formalism within the independent particle approximation.[60,61] The second-order NLO susceptibility can be expressed as

$$\chi_{abc} L(-2\omega; \omega, \omega) = \chi_{abc} \text{inter}(-2\omega; \omega, \omega) + \chi_{abc} \text{inter}(-2\omega; \omega, \omega) + \chi_{abc} \text{mod}(-2\omega; \omega, \omega)$$

where the subscript L denotes the length gauge, and χ_{abc} inter, χ_{abc} intra and χ_{abc} mod give the contributions to $\chi_{abc} L$ from interband processes, intraband processes, and the modulation of interband terms by intraband terms, respectively.

The convergence test of the SHG coefficient upon k-point sampling and empty bands with $H_{11}C_4N_2CdI_3$ as an example was carried out (Table S9†), and we found that the SHG coefficient gradually converges when the k-point separation is not more than 0.04 $Å^{-1}$ ($2 \times 3 \times 2$) and the quantity of the empty bands is not less than 2 times that of valence bands (280 bands). So the choice of k-point sampling and the empty band number during the optical property calculation is reasonable.

Results and discussion

In order to investigate the differences in the synthesis conditions of $H_{12}C_4N_3CdI_4$ and $H_{11}C_4N_2CdI_3$, we conducted multiple sets of control experiments as shown in Table S1.† Several observations were made: (1) the molar ratio of Cd to $H_{10}C_4N_2$ had no impact on whether $H_{12}C_4N_3CdI_4$ or $H_{11}C_4N_2CdI_3$ was produced as the final product; (2) changes in temperature had minimal effects on the synthesis of $H_{12}C_4N_3CdI_4$; (3) the ratio of HI to H_2O was the determining factor in the preparation of $H_{12}C_4N_3CdI_4$ or $H_{11}C_4N_2CdI_3$. We hypothesize that a lower HI : H_2O ratio can reduce the concentration of iodide ions in the reaction system, thus facilitating direct coordination bonding between Cd^{2+} cations and $H_{10}C_4N_2$, resulting in the formation of $H_{11}C_4N_2CdI_3$; (4) in the preparation process of $H_{11}C_4N_2CdI_3$, Y_2O_3 is essential and cannot be omitted. However, indeed, the specific role of Y_2O_3 in the synthesis process of $H_{11}C_4N_2CdI_3$ is currently unclear due to limitations in our current technological means. Their measured powder XRD patterns are consistent with those of simulated data, confirming the phase purity (Fig. S1†). The EDS results of the Cd : I ratios are 1.0 : 4.10 and 1.0 : 2.97 for $H_{12}C_4N_2CdI_4$ and $H_{11}C_4N_2CdI_3$, respectively (Fig. S2†). In addition, elemental analysis of C, N, and H atoms is provided in Table S6† with weight%: C 6.77, H 1.63, and N 4.02 for $H_{12}C_4N_2CdI_4$; C 8.30, H 1.85, and N 4.53 for $H_{11}C_4N_2CdI_3$ (Table S7†). Both of them are in good agreement with the crystal structure solution.

Crystal structure

$H_{12}C_4N_2CdI_4$ crystallizes in a noncentrosymmetric space group $P2_12_12_1$ (No. 19) with one cationic $H_{12}C_2N_4^{2+}$ (H_2PIP^{2+}) six-membered ring and one anionic CdI_4^{2-} tetrahedron in each asymmetric unit (Fig. 1). In the $H_{12}C_4N_2$-ring, each C and N atom exhibits sp^3 hybridization, with C–N/C–C distances of 1.49(2)–1.50(2) Å and 1.474(17)–1.496(18) Å, respectively. The bond angles in the $H_{12}C_4N_2$-ring range from 110.5(12)–111.2(11)°, which is consistent with those of previously reported piperazine compounds.[62,63] As a result, the $H_{12}C_2N_4^{2+}$ cation takes on a chair conformation, rather than a planar π-conjugated structure. Each Cd^{2+} cation bonds with four I^- anions to form a CdI_4 tetrahedron, with Cd–I distances ranging from 2.7548(14)–2.8089(14) Å and I–Cd–I angles of 104.50(4)–113.75(5)°. Neighboring $H_{12}C_2N_4$ and CdI_4 groups are isolated from each other and arranged in a quasi-two-dimensional (quasi-2D) [$H_{12}C_4N_2CdI_4$] layer (Fig. 1c), parallel to the ac plane. These pseudo-layers stack along the b direction to form the entire 3D network of $H_{12}C_4N_2CdI_4$ (Fig. 1d).

$H_{11}C_4N_2CdI_3$ crystallizes in the polar space group Cc (No. 9), with an asymmetric unit including one protonated-piperazine
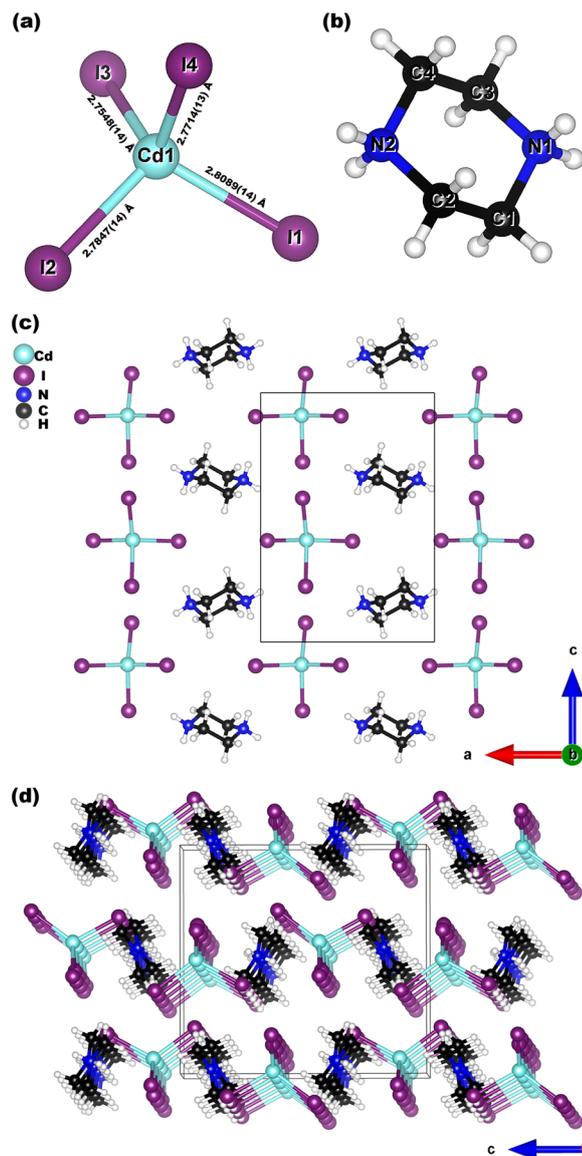
Fig. 1 Views of the structures of the CdI_4 tetrahedron (a), the chair shaped H_2PIP^{2+} cation (b), the quasi-2D $H_{12}C_2N_4CdI_4$ layer along the b-axis (c) and $H_{12}C_2N_4CdI_4$ along the a-axis (d).

Fig. 2 Views of the structures of the $H_{11}C_4N_2CdI_3$ molecule (a), the quasi-2D $H_{11}C_4N_2CdI_3$ layer along the a-axis (b) and $H_{11}C_4N_2CdI_3$ along the b-axis.

group, one Cd, and three I atoms (Fig. 2a). In the chair-shaped $H_{11}C_4N_2$-ring, C–N and C–C distances are 1.49(2)–1.532(17) Å and 1.462(17)–1.509(19) Å, respectively, and the bond angles are in the range of 108.7(11)–114.5(9)°, which are consistent with those of previously reported piperazine compounds.[62,63] Each Cd^{2+} cation connects with one N atom and three I atoms to form a *N*-hybrid polyhedron, a $CdNI_3$ tetrahedron. The length of Cd–N (2.300(11) Å) is smaller than those of Cd–I (2.7393(12)–2.7518(11) Å), and the bond angles of N–Cd–I and I–Cd–I are 100.8(3)–104.0(3)° and 112.80(3)–117.07(4)°, respectively. Furthermore, one $H_{11}C_4N_2$-ring is connected with one $CdNI_3$ tetrahedron *via* the corner-sharing of N atoms, forming a H_{11}-$C_4N_2CdI_3$ molecule (Fig. 2a). Neighboring $H_{11}C_4N_2CdI_3$ molecules are interconnected in a quasi-1D zigzag chain along the *c*-direction, which is further arranged in quasi-2D layers parallel
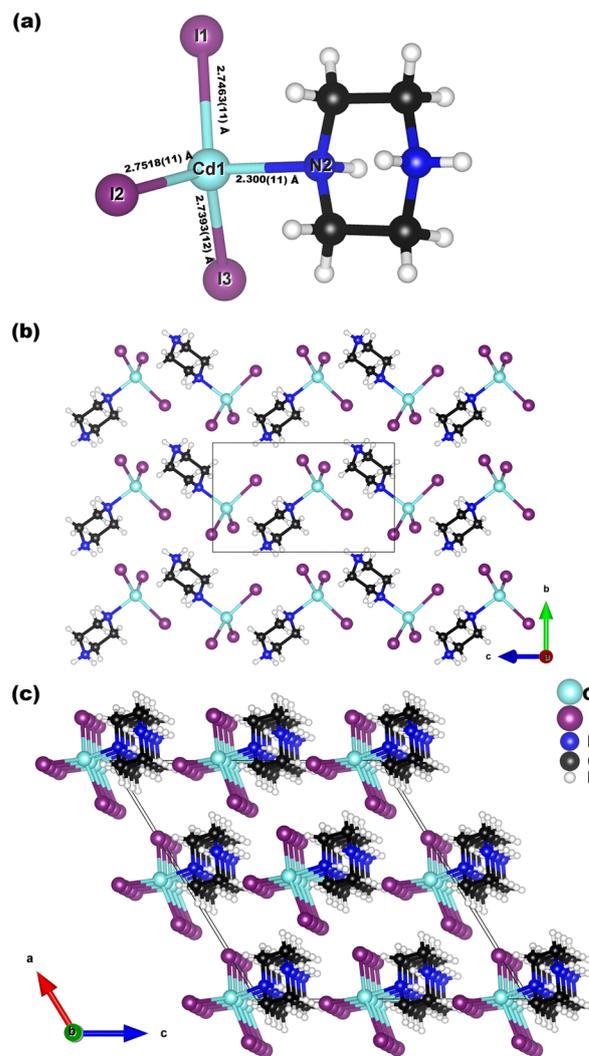
to the *bc* plane (Fig. 2b). These quasi-2D layers are stacked upward along the *a*-axis, resulting in the structure of $H_{11}C_4N_2CdI_3$ (Fig. 2c).

Structural comparison

It is interesting to compare the structural differences of the title compounds to further understand why $H_{11}C_4N_2CdI_3$ is a polar compound while $H_{12}C_4N_2CdI_4$ is not. Firstly, we believe that the distinct coordination environments of Cd^{2+} ions play a key role. In $H_{12}C_4N_2CdI_4$, the molar ratio of Cd to I is 4, which results in each Cd^{2+} ion being surrounded by only four I atoms, forming a nearly undistorted CdI_4 tetrahedron. In contrast, in $H_{11}C_4N_2CdI_3$, Cd: I is 3, which enables the N atom on the $H_{10}C_4N_2$ unit to participate in Cd^{2+} coordination, forming a distorted $CdNI_3$ tetrahedron. Secondly, the calculated dipole moments of the CdI_4 and $CdNI_3$ units are 3.27 and 5.94 *D* (Table S10†), respectively, indicating that $CdNI_3$ exhibits more anisotropy, favoring the formation of a polar structure. Finally,

the arrangement of Cd^{2+}-centered tetrahedra can also affect the polarity. In $H_{12}C_4N_2CdI_4$, each $H_{12}C_4N_2^{2+}$ cation is surrounded by four CdI_4 tetrahedra, and their dipole moments cancel out each other along the a, b, and c axes (Table S10†). As a result, although $H_{12}C_4N_2CdI_4$ has a noncentrosymmetric structure, it is nonpolar, and its net dipole moment in a unit cell is zero. However, in $H_{11}C_4N_2CdI_3$, the dipole moments of $CdNI_3$ tetrahedra cancel out each other only along the b axis, while they add up along the a and c axes, resulting in a large net dipole moment of about 17.09 D (Table S10†). Therefore, $H_{11}C_4N_2CdI_3$ is a noncentrosymmetric and polar compound.

Thermal and optical properties

Thermogravimetric analysis (TGA) shows the good thermal stabilities of $H_{12}C_4N_2CdI_4$ and $H_{11}C_4N_2CdI_3$, at around 300 °C (Fig. 3a). These values are higher than those of previously reported NLO organic–inorganic halides, including $(H_7C_3N_6)(H_6C_3N_6)HgCl_3$ (225 °C),[16] $(CH_3NH_3)GeBr_3$ (500 K),[30] $[C_{18}H_{21}N_4][AgI_3]I$ (260 °C)[18] and $Rb_2[PbI_2(HCOO)_2]$ (240 °C).[64] The UV-vis spectra show the absorption edges of 291 and 289 nm for $H_{12}C_4N_2CdI_4$ and $H_{11}C_4N_2CdI_3$, respectively (Fig. S4†). Furthermore, compared to $H_{12}C_4N_2CdI_4$, $H_{11}C_4N_2CdI_3$ exhibits a slightly larger bandgap (4.10 eV $vs.$ 3.86 eV) (Fig. 3b), which can primarily be attributed to a reduction in the number of I^- ions. Besides, the bandgaps of $H_{12}C_4N_2CdI_4$ and $H_{11}C_4N_2CdI_3$ are wider than that of the NLO o-containing SCALP cation, such as $(C_4H_{10}NO)PbCl_3$ (3.55 eV),[65] $(C_7H_{15}NCl)SbCl_4$ (3.05 eV),[66] $(C_6H_5(CH_2)_4NH_3)_4BiI_7 \cdot H_2O$ (2.29 eV),[41] $Rb_2[PbI_2(HCOO)_2]$ (240 °C) (3.40 eV),[64] $(R/S-C_{16}H_{22}N_2Cl)_2$-$SnCl_6$ (3.39 eV)[67] and $(CH_3NH_3)GeBr_3$ (2.91 eV).[30]

SHG properties

Since both $H_{12}C_4N_2CdI_4$ and $H_{11}C_4N_2CdI_3$ are non-centrosymmetric, their SHG effects are measured according to the method of Kurtz and Perry.[55] For $H_{12}C_4N_2CdI_4$, as shown in Fig. S5,† the measurement result reveals unwanted non-phase matchable NLO properties, in which the SHG intensity of the crystalline samples exhibits an initial increase, followed by a subsequent decrease as the particle size increased. The maximum value, which is approximately 90 μm, is observed to be about 0.5 times that of KH_2PO_4 (KDP). This phenomenon is reminiscent of the behavior exhibited by traditional phosphate and sulfate compounds, where the CdI_4 tetrahedron exhibits minimal distortion, and its optical anisotropy is mutually canceled within the $P2_12_12_1$ space group. Conversely, as shown in Fig. 3c and d, the SHG intensity gradually increased and saturated with increasing particle size, indicating that $H_{11}C_4N_2CdI_3$ exhibits phase-matching NLO properties. The SHG effect of $H_{11}C_4N_2CdI_3$ is about six times that of KDP, measured at a particle size of 150–210 μm.

It is interesting to investigate the structure–property relationship among the title compounds and formerly reported Cd-centered NLO OIMHs, such as $[(CH_3)_3NCH_2Cl]CdCl_3$,[46] $(H_{10}C_4NO)_2Cd_2Cl_6$,[42] (L/D-Hpro)$_2Cd_5Cl_{12}$,[43] (L/D-Hpro)(L-pro)$CdCl_3$,[43] and L/D-$C_{12}H_{20}N_6O_4Cd_2Cl_5$.[44] The structure of $[(CH_3)_3NCH_2Cl]CdCl_3$ contains a 0D $CdCl_6$ octahedron, whereas in (L/D-Hpro)$_2Cd_5Cl_{12}$ and (L/D-Hpro)(L-pro)$CdCl_3$, the $CdCl_6$ octahedra are interconnected into the 2D Cd_5Cl_{12} layer via edge-sharing and the 1D $CdCl_3$ chain via face-sharing, respectively. Notably, such $CdCl_6$ octahedra only exhibit low optical anisotropy, with very small dipole moments (<0.1 D). Hence, their SHG response is relatively weak (<1.0 × KDP). Besides, the N/O atoms in non-π-
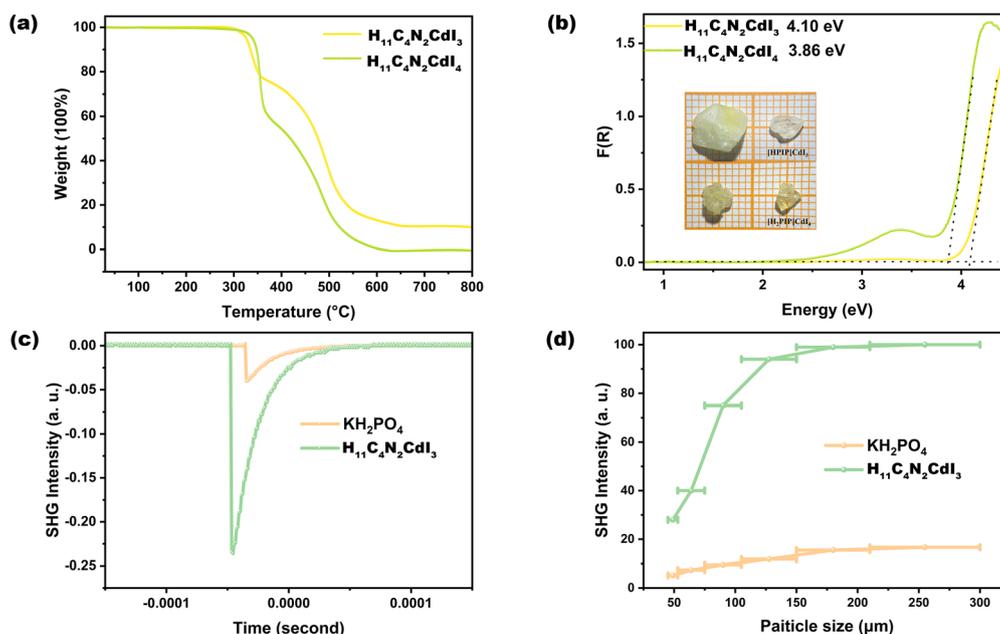

Fig. 3 TGA curves (a), UV-vis diffuse reflectance spectra (inset picture is the crystal photo) (b), measured oscilloscope traces of the SHG signals (150–210 mm) (c) and SHG intensity $vs.$ particle size of compounds under 1064 nm laser radiation (d). KDP served as the reference.

conjugated organic groups are sp^3 hybridized, which makes them more likely to form coordination bonds with Cd^{2+} cations in non-π-conjugated OIMHs. Therefore, many of them feature an O/N-hybridized polyhedron. In (H$_{10}$C$_4$NO)$_2$Cd$_2$Cl$_6$, neighbouring CdCl$_6$ and CdCl$_4$O$_2$ octahedra are bridged into a 1D chain via edge-sharing. L/D-C$_{12}$H$_{20}$N$_6$O$_4$Cd$_2$Cl$_5$ contains a CdOCl$_4$ trigonal bipyramid, and each pair of them is formed into a Cd$_2$O$_2$Cl$_6$ dimer via edge-sharing. Importantly, these Cd–O–Cl polyhedra feature larger dipole moments (1.14–5.03 D) that a CdCl$_6$ octahedron. However, for example, the undesired arrangement of CdOCl$_4$ groups leads to a small net dipole moment (1.19–1.20 D) and weak SHG response in L/D-C$_{12}$H$_{20}$N$_6$O$_4$Cd$_2$Cl$_5$ (~0.2 × KDP). Most importantly, in this work, H$_{12}$C$_4$N$_2$CdI$_4$ and H$_{11}$C$_4$N$_2$CdI$_3$ involve CdI$_4$ (3.27 D) and CdNI$_3$ (5.94 D) tetrahedra, respectively, in which the polarization magnitudes of CdNI$_3$ tetrahedra are mutually superimposed along the a- and c-axes resulting in a large net dipole moment of H$_{11}$C$_4$N$_2$CdI$_3$ (17.09 D) (Table S10†). Accordingly, compared with previously reported Cd-centered OIMHs and H$_{12}$C$_4$N$_2$CdI$_4$, H$_{11}$C$_4$N$_2$CdI$_3$ features a far large SHG response (6 × KDP).

Besides, importantly, compared with recently reported NLO OIMHs with SCALP or other d^{10}-TM cations such as (C$_4$H$_{10}$NO)PbBr$_3$ (0.81 × KDP),[65] [C(NH$_2$)$_3$]SbF$_4$ (2 × KDP),[32] [N(CH$_3$)$_4$]HgBrI$_2$ (4.5 × KDP),[68] (H$_7$C$_3$N$_6$)(H$_6$C$_3$N$_6$)HgCl$_3$ (5.8 × KDP),[16] α-(CN$_3$H$_6$)$_3$Cu$_2$I$_5$ (1.8 × KDP),[19] (CH$_3$NH$_3$)GeBr$_3$ (5.3 × KDP)[30] and (C$_{20}$H$_{20}$P)CuCl$_2$ (1.1 × KDP),[69] H$_{11}$C$_4$N$_2$CdI$_3$ has a stronger SHG response (6 × KDP). Furthermore, the SHG responses and bandgaps of selected organic–inorganic halides are summarized in Fig. 4 and Table S11† (the relevant references are provided in the ESI†). Unlike other NLO crystals, H$_{11}$C$_4$N$_2$CdI$_3$ simultaneously exhibits both a strong SHG effect (>5 × KDP) and wide bandgap (>4.0 eV), which makes it promising as a high-performance ultraviolet NLO crystal.

Structure–property relationship analysis

The calculated bandgaps of H$_{12}$C$_4$N$_2$CdI$_4$ and H$_{11}$C$_4$N$_2$CdI$_3$ are provided in Fig. S6,† indicating that they are direct bandgap

compounds with values of 3.895 and 4.102 eV for H$_{12}$C$_4$N$_2$CdI$_4$ and H$_{11}$C$_4$N$_2$CdI$_3$, respectively, being comparable to the results from measurement (3.86 and 4.10 eV). Partial density of states (PDOS) of H$_{12}$C$_4$N$_2$CdI$_4$ and H$_{11}$C$_4$N$_2$CdI$_3$ is presented in Fig. 5a and b, respectively. The PDOS plots of both compounds are similar. The contribution to the valence band maximum (VBM) mainly comes from the I-p orbitals, as well as a small portion of the Cd-p orbitals. For the conduction band minimum (CBM), the contribution sizes rank in the order of Cd-s, I-p, and I-s orbitals. It is worth noting that in H$_{11}$C$_4$N$_2$CdI$_3$, a small amount of N-p orbitals also contributes to the VBM, which is consistent with the existence of the Cd–N bond. Therefore, we believe that the bandgaps of H$_{12}$C$_4$N$_2$CdI$_4$ and H$_{11}$C$_4$N$_2$CdI$_3$ are determined by the Cd-centered tetrahedra.

Herein, we use the calculated birefringence (Δn) and phase matching wavelength based on the relations between the wavelength and refractive index under both fundamental and harmonic conditions (Fig. 6). Both of them are biaxial crystals with three principal optical axes, i.e., X, Y, and Z. For the orthorhombic crystal H$_{12}$C$_4$N$_2$CdI$_4$, the calculated refractive index curves after structure optimization show the order of $n_c > n_a > n_b$ in the low-frequency range, and to satisfy the biaxial condition $n_X > n_Y > n_Z$, the transformation of $c → x$, $a → y$, and $b → z$ is performed and a correct order of $n_X > n_Y > n_Z$ is shown in Fig. 6a. For the monoclinic crystal H$_{11}$C$_4$N$_2$CdI$_3$, the crystallographic axes and principal dielectric axes are not consistent with each other in the ac plane, so the principal dielectric axes in the ac plane must be determined after structure optimization and before the optical calculation. According to the principal axis transformation method in our previous work, the rotation angle θ between the
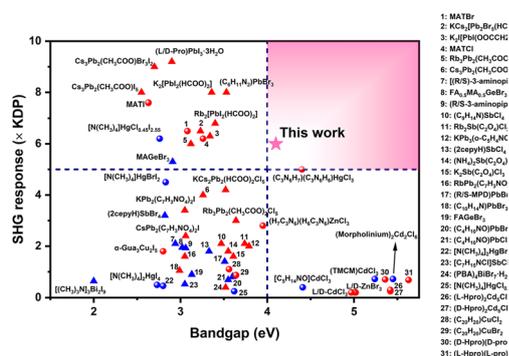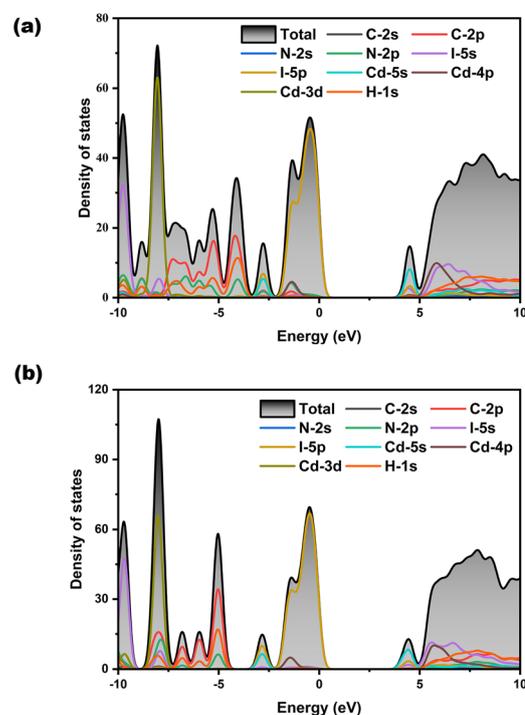

Fig. 4 SHG response and energy bandgap of representative NLO organic−inorganic halides. Red ball: compound containing both a π-conjugated organic group and SCALP cation, red triangle: compound containing a π-conjugated organic group but without a SCALP cation, blue ball: compound without a π-conjugated organic group but with a SCALP cation, blue triangle: other compounds.

Fig. 5 The density of states of H$_{12}$C$_4$N$_2$CdI$_4$ and H$_{11}$C$_4$N$_2$CdI$_3$ (b).

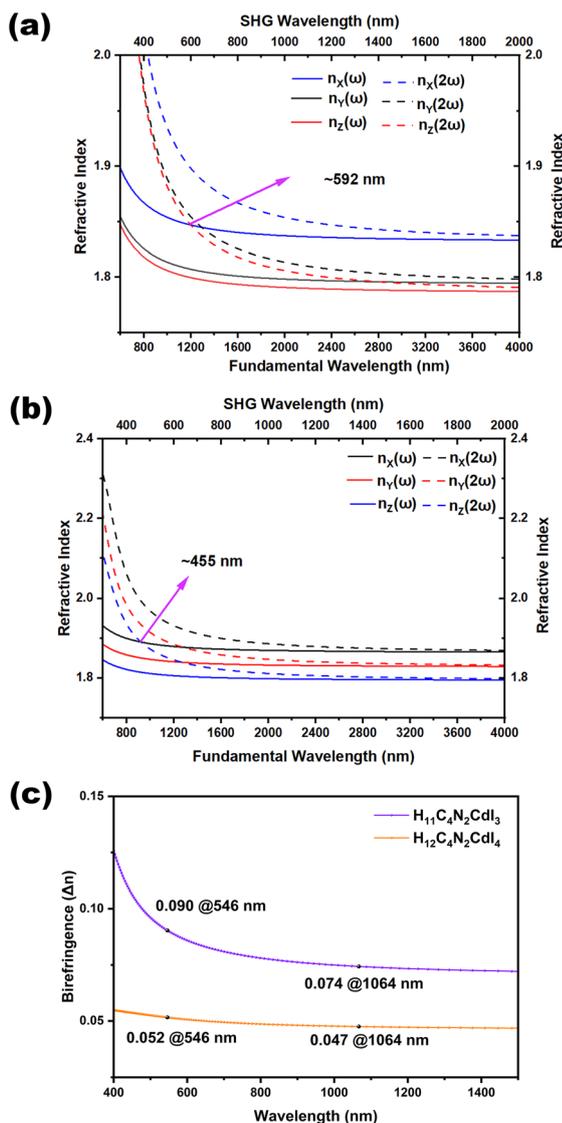**Fig. 6** Refractive index dispersion curves for fundamental and second-harmonic light of $H_{12}C_4N_2CdI_4$ (a) and $H_{11}C_4N_2CdI_3$ (b), as well as the calculated birefringence (c). The type-I phase matching wavelengths in different planes were evaluated based on the calculated refractive index, in which we consider the type-I phase matching condition of $n(\omega) = n(2\omega)$.

original coordinate axes (*i.e.* $y\|b$, $z\|c$) and the principal dielectric axes is found to be 25.179°.[70] After the principal axis transformation and based on the principal dielectric coordinate system, the calculated refractive index curves show an order of $n_X > n_Y > n_Z$ and satisfy the biaxial condition. The shortest wavelengths for type-I phase matching are approximately 592 nm and 466 nm for $H_{12}C_4N_2CdI_4$ and $H_{11}C_4N_2CdI_3$, respectively. This implies that under 1064 nm laser radiation, $H_{11}C_4N_2CdI_3$ can achieve type-I phase matching, while $H_{12}C_4N_2CdI_4$ cannot. These findings are consistent with our SHG measurements. These calculated birefringences have been obtained from the refractive index difference ($n_X - n_Z$) (Fig. 6c), in which $H_{11}C_4N_2CdI_3$ possesses a larger birefringence of (0.090 @546 nm, 0.074 @1064

nm) than that of $H_{12}C_4N_2CdI_4$ (0.052 @546 nm, 0.047 @1064 nm). Since piperazine is a non-π conjugated group with negligible contribution of birefringence, the larger birefringence of $H_{11}C_4N_2CdI_3$ can be attributed to the microscopic asymmetry and well-arranged structure of the $CdNI_3$ group, exemplified by the dipole moment calculation (Table S10†). Consequently, from $H_{12}C_4N_2CdI_4$ to $H_{11}C_4N_2CdI_3$, the polarizable $CdNI_3$ tetrahedron induces an enlarged birefringence, ensuring phase-matching performance of $H_{11}C_4N_2CdI_3$.

We further calculate the theoretical SHG coefficients of $H_{12}C_4N_2CdI_4$ and $H_{11}C_4N_2CdI_3$, as shown in Table S12.† For $H_{12}C_4N_2CdI_4$, it has three non-zero independent SHG tensors with the same value of 0.12 pm V^{-1}, which is about 0.3 times that of KDP (0.39 pm V^{-1}), being consistent with the experimental value (0.5 × KDP). More importantly, for $H_{11}C_4N_2CdI_3$, its largest independent SHG tensor is $d_{11} = 2.74$ pm V^{-1}, about 7 times larger than that of KDP, which is agreement with the experimental result (6 × KDP). To explore the origin of the better SHG effect of $H_{11}C_4N_2CdI_3$, we further calculated the SHG density distribution of the d_{11} tensor (Fig. 7). In the VB, the main source of the SHG effect is the I-5p states. In addition, there are small contributions from the Cd 5s states and the N-2p states from the Cd–N bond. The maximum source in the CB is the Cd-5s orbitals, followed by the I-5s orbitals and the N-2p orbitals in the Cd–N bond. Furthermore, the contributions of each unit to the SHG response are calculated, and the $CdNI_3$ tetrahedron has a contribution as high as 97.96%. Therefore, we believe that the distorted $CdNI_3$ tetrahedron is the primary origin of the outstanding SHG effect of $H_{11}C_4N_2CdI_3$.
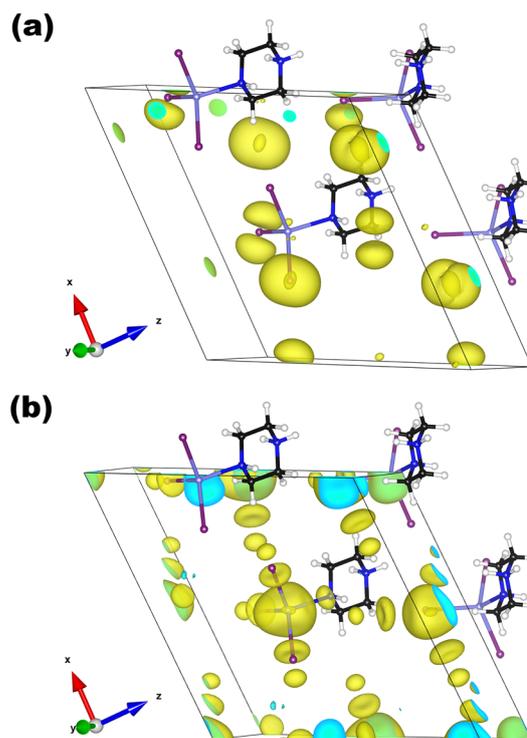

Fig. 7 SHG density plots for $H_{11}C_4N_2CdI_3$: VB (a) and CB (b).

Conclusions

In summary, we have discovered two new organic–inorganic metal halides (OIMHs), $H_{12}C_4N_2CdI_4$ and $H_{11}C_4N_2CdI_3$, by combining the protonated pyrazine cation with d^{10}-TM-halide tetrahedra. The NLO properties of non-π-conjugated piperazine compounds are studied for the first time. Despite being a noncentrosymmetric compound, $H_{12}C_4N_2CdI_4$ exhibits a weak and non-phase-matchable SHG effect. In contrast, $H_{11}C_4N_2CdI_3$ is a polar compound with excellent NLO performance, including a strong SHG response ($6 \times$ KDP), a wide bandgap (4.10 eV), large birefringence (0.074 @1064 nm) for phase-matching requirement, good thermal stability (300 °C), and a suitable crystal growth habit. The structure–property relationship analysis indicates that the highly polarizable N-hybridized $CdNI_3$ tetrahedron in the $H_{11}C_4N_2CdI_3$ structure is the primary cause of the birefringence and SHG effect. Our work provides new insights for exploring semi-organic NLO crystals that do not contain π-conjugated organic components. Further exploration of OIMHs containing N- or O-hybridized metal-halide polyhedra is currently underway.

Data availability

The experimental or computational data can be obtained *via* contacting the corresponding author.

Author contributions

Wu Huai-Yu: conceptualization, methodology, writing – original draft, data curation , visualization; Xu Miao-Bin, Chen Qian-Qian, and Ma Nan: data curation; Hu Chun-Li: formal analysis; Huang Xiao-Ying, Du Ke-Zhao and Chen Jin: writing – review & editing, supervision.

Conflicts of interest

There are no conflicts to declare.

Acknowledgements

References

1 M. Mutailipu, K. R. Poeppelmeier and S. Pan, Borates: A Rich Source for Optical Materials, *Chem. Rev.*, 2021, **121**, 1130–1202.

2 J. Chen, C. L. Hu, F. Kong and J. G. Mao, High-Performance Second-Harmonic-Generation (SHG) Materials: New Developments and New Strategies, *Acc. Chem. Res.*, 2021, **54**, 2775–2783.

3 L. Kang, F. Liang, X. Jiang, Z. Lin and C. Chen, First-Principles Design and Simulations Promote the Development of Nonlinear Optical Crystals, *Acc. Chem. Res.*, 2020, **53**, 209–217.

4 M. Mutailipu and S. Pan, Emergent Deep-Ultraviolet Nonlinear Optical Candidates, *Angew. Chem., Int. Ed.*, 2019, **59**, 20302–20317.

5 X. Chen and K. M. Ok, Metal oxyhalides: an emerging family of nonlinear optical materials, *Chem. Sci.*, 2022, **13**, 3942–3956.

6 L. Cao, H. Tian, D. Lin, C. Lin, F. Xu, Y. Han, T. Yan, J. Chen, B. Li, N. Ye and M. Luo, A flexible functional module to regulate ultraviolet optical nonlinearity for achieving a balance between a second-harmonic generation response and birefringence, *Chem. Sci.*, 2022, **13**, 6990–6997.

7 K. M. Ok, Toward the Rational Design of Novel Noncentrosymmetric Materials: Factors Influencing the Framework Structures, *Acc. Chem. Res.*, 2016, **49**, 2774–2785.

8 Y. Pan, S.-P. Guo, B.-W. Liu, H.-G. Xue and G.-C. Guo, Second-order nonlinear optical crystals with mixed anions, *Coord. Chem. Rev.*, 2018, **374**, 464–496.

9 W. Wang, D. Mei, S. Wen, J. Wang and Y. Wu, Complex coordinated functional groups: a great genes for nonlinear optical materials, *Chin. Chem. Lett.*, 2022, **33**, 2301–2315.

10 C. Wu, T.-H. Wu, X.-X. Jiang, Z.-J. Wang, H.-Y. Sha, L. Lin, Z.-S. Lin, Z.-P. Huang, X.-F. Long, M. G. Humphrey and C. Zhang, Large Second-Harmonic Response and Giant Birefringence of $CeF_2(SO_4)$ Induced by Highly Polarizable Polyhedra, *J. Am. Chem. Soc.*, 2021, **143**, 4138–4142.

11 D. Lin, M. Luo, C. Lin, F. Xu and N. Ye, $KLi(HC_3N_3O_3).2H_2O$: Solvent-drop Grinding Method toward the Hydro-isocyanurate Nonlinear Optical Crystal, *J. Am. Chem. Soc.*, 2019, **141**, 3390–3394.

12 X. Meng, X. Zhang, Q. Liu, Z. Zhou, X. Jiang, Y. Wang, Z. Lin and M. Xia, Perfectly Encoding pi-Conjugated Anions in the $RE_5(C_3N_3O_3)(OH)_{12}$ (RE = Y, Yb, Lu) Family with Strong Second Harmonic Generation Response and Balanced Birefringence, *Angew. Chem., Int. Ed.*, 2023, **62**, e202214848.

13 M. Luo, C. Lin, D. Lin and N. Ye, Rational Design of the Metal-Free $KBe_2BO_3F_2$ (KBBF) Family Member $C(NH_2)_3SO_3F$ with Ultraviolet Optical Nonlinearity, *Angew. Chem., Int. Ed.*, 2020, **59**, 15978–15981.

14 J. Lu, X. Liu, M. Zhao, X. B. Deng, K. X. Shi, Q. R. Wu, L. Chen and L. M. Wu, Discovery of NLO Semiorganic $(C_5H_6ON)^+(H_2PO_4)^-$: Dipole Moment Modulation and Superior Synergy in Solar-Blind UV Region, *J. Am. Chem. Soc.*, 2021, **143**, 3647–3654.

15 Q. Q. Chen, C. L. Hu, J. Chen, Y. L. Li, B. X. Li and J. G. Mao, $[o-C_5H_4NHOH]_2[I_7O_{18}(OH)]$ $3H_2O$: An Organic-Inorganic Hybrid SHG Material Featuring an $[I_7O_{18}(OH)]$ infinity2-Branched Polyiodate Chain, *Angew. Chem., Int. Ed.*, 2021, **60**, 17426–17429.

16 Z. Bai, J. Lee, H. Kim, C. L. Hu and K. M. Ok, Unveiling the Superior Optical Properties of Novel Melamine-Based Nonlinear Optical Material with Strong Second-Harmonic Generation and Giant Optical Anisotropy, *Small*, 2023, e2301756, DOI: **10.1002/smll.202301756**.

17 L. Liu, Z. Bai, L. Hu, D. Wei, Z. Lin and L. Zhang, A melamine-based organic–inorganic hybrid material revealing excellent optical performance and moderate thermal stability, *J. Mater. Chem. C*, 2021, **9**, 7452–7457.

18 X. Y. Li, Q. Wei, C. L. Hu, J. Pan, B. X. Li, Z. Z. Xue, X. Y. Li, J. H. Li, J. G. Mao and G. M. Wang, Achieving Large Second Harmonic Generation Effects via Optimal Planar Alignment of Triangular Units, *Adv. Funct. Mater.*, 2022, **33**, 2210718.

19 J. Wu, Y. Guo, J. L. Qi, W. D. Yao, S. X. Yu, W. Liu and S. P. Guo, Multi-Stimuli Responsive Luminescence and Domino Phase Transition of Hybrid Copper Halides with Nonlinear Optical Switching Behavior, *Angew. Chem., Int. Ed.*, 2023, **62**, e202301937.

20 Y. Deng, X. Dong, M. Yang, H. Zeng, G. Zou and Z. Lin, Two low-dimensional metal halides: ionothermal synthesis, photoluminescence, and nonlinear optical properties, *Dalton Trans.*, 2019, **48**, 17451–17455.

21 Y. Li, J. Luo and S. Zhao, Local Polarity-Induced Assembly of Second-Order Nonlinear Optical Materials, *Acc. Chem. Res.*, 2022, **55**, 3460–3469.

22 M. Mutailipu, Z. Yang and S. Pan, Toward the Enhancement of Critical Performance for Deep-Ultraviolet Frequency-Doubling Crystals Utilizing Covalent Tetrahedra, *Acc. Mater. Res.*, 2021, **2**, 282–291.

23 X. Meng, W. Yin and M. Xia, Cyanurates consisting of intrinsic planar π-conjugated 6-membered rings: an emerging source of optical functional materials, *Coord. Chem. Rev.*, 2021, **439**, 213916.

24 S. Hongkang, Y. Ziting, H. Xueling and Z. Min, Fluorooxoborates: a precious treasure of deep-ultraviolet nonlinear optical materials, *Chin. J. Struct. Chem.*, 2023, **42**, 100027.

25 Z. Boxuan and C. Zhaohui, Recent advances of inorganic phosphates with UV/DUV cutoff edge and large second harmonic response, *Chin. J. Struct. Chem.*, 2023, **42**, 100033.

26 L. Qing-Fen, C. Wei-Feng, L. You-Zhao and C. Jian-Wen, Recent progress in ultraviolet and deep-ultraviolet nonlinear optical aluminoborates, *Chin. J. Struct. Chem.*, 2023, **42**, 100036.

27 C. Xu, L. Yanqiang, L. Junhua and Z. Sangen, Recent advances in non-π-conjugated nonlinear optical sulfates with deep-UV absorption edge, *Chin. J. Struct. Chem.*, 2023, **42**, 100044.

28 F. Wu, Q. Wei, X. Li, Y. Liu, W. Huang, Q. Chen, B. Li, J. Luo and X. Liu, Cooperative Enhancement of Second Harmonic Generation in an Organic–Inorganic Hybrid Antimony Halide, *Cryst. Growth Des.*, 2022, **22**, 3875–3881.

29 S. Qi, P. Cheng, X. Han, F. Ge, R. Shi, L. Xu, G. Li and J. Xu, Organic–Inorganic Hybrid Antimony(III) Halides for Second Harmonic Generation, *Cryst. Growth Des.*, 2022, **22**, 6545–6553.

30 Y. Liu, Y. P. Gong, S. Geng, M. L. Feng, D. Manidaki, Z. Deng, C. C. Stoumpos, P. Canepa, Z. Xiao, W. X. Zhang and L. Mao, Hybrid Germanium Bromide Perovskites with Tunable Second Harmonic Generation, *Angew. Chem., Int. Ed.*, 2022, **61**, e202208875.

31 X. Li, Y. Guan, X. Li and Y. Fu, Stereochemically Active Lone Pairs and Nonlinear Optical Properties of Two-Dimensional Multilayered Tin and Germanium Iodide Perovskites, *J. Am. Chem. Soc.*, 2022, **144**, 18030–18042.

32 W. Zhang, W. Jin, S. Han, Z. Yang and S. Pan, $Pb_3Ba_7B_7O_{20}F$: a new nonlinear optical material exhibiting large second harmonic generation response induced by its unprecedented Pb-B-O framework, *Scr. Mater.*, 2021, **194**, 113700.

33 Z. Qi, Y. Chen, H. Gao, F.-Q. Zhang, S.-L. Li and X.-M. Zhang, Two SbX_5-based isostructural polar 1D hybrid antimony halides with tunable broadband emission, nonlinear optics, and semiconductor properties, *Sci. China: Chem.*, 2021, **64**, 2111–2117.

34 K. Liu, C. Deng, C. Li, X. Zhang, J. Cao, J. Yao, J. Zhao, X. Jiang, Z. Lin and Q. Liu, Hybrid Metal-Halide Infrared Nonlinear Optical Crystals of $(TMEDA)MI_5$ (M = Sb, Bi) with High Stability, *Adv. Opt. Mater.*, 2021, **9**, 2101333.

35 J.-H. Wu, B. Zhang, T.-K. Jiang, F. Kong and J.-G. Mao, From $Cs_8Sb_4Nb_5O_5F_{35}$ to $Cs_6Sb_4Mo_3O_5F_{26}$: the first noncentrosymmetric fluoroantimonite with d0 transition metal, *Chin. J. Struct. Chem.*, 2023, **42**, 100016.

36 J. Chen, C.-L. Hu, Y.-L. Lin, Y. Chen, Q.-Q. Chen and J.-G. Mao, $K_3V_2O_3F_4(IO_3)_3$: a high-performance SHG crystal containing both five and six-coordinated V^{5+} cations, *Chem. Sci.*, 2022, **13**, 454–460.

37 J. Chen and K.-Z. Du, $ZrF_2(IO_3)_2$ and $RbGaF_3(IO_3)$: Two Promising Birefringent Crystals Featuring 1D Metal-Fluoride Cationic Chains and Wide Bandgaps, *Inorg. Chem.*, 2022, **61**, 17893–17901.

38 J. Chen, C.-L. Hu, X.-H. Zhang, B.-X. Li, B.-P. Yang and J.-G. Mao, $CsVO_2F(IO_3)$: An Excellent SHG Material Featuring an Unprecedented 3D $[VO_2F(IO_3)]^-$ Anionic Framework, *Angew. Chem., Int. Ed.*, 2020, **59**, 5381–5384.

39 J. Chen, C.-L. Hu, F.-F. Mao, B.-P. Yang, X.-H. Zhang and J.-G. Mao, REI_5O_{14} (RE = Y and Gd): Promising SHG Materials Featuring the Semicircle-Shaped $I_5O_{14}^{3-}$ Polyiodate Anion, *Angew. Chem., Int. Ed.*, 2019, **58**, 11666–11669.

40 J. Chen, C.-L. Hu, F.-F. Mao, J.-H. Feng and J.-G. Mao, A Facile Route to Nonlinear Optical Materials: Three-Site Aliovalent Substitution Involving One Cation and Two Anions, *Angew. Chem., Int. Ed.*, 2019, **58**, 2098–2102.

41 D. Chen, S. Hao, L. Fan, Y. Guo, J. Yao, C. Wolverton, M. G. Kanatzidis, J. Zhao and Q. Liu, Broad Photoluminescence and Second-Harmonic Generation in the Noncentrosymmetric Organic–Inorganic Hybrid Halide $(C6H5(CH2)4NH3)4MX7·H2O$ (M = Bi, In, X = Br or I), *Chem. Mater.*, 2021, **33**, 8106–8111.

42 D. Sun, D. Wang, Y. Dang, S. Zhang, H. Chen, R. Hou, K. Wu and C. Shen, Organic-Inorganic Hybrid Noncentrosymmetric $(Morpholinium)_2Cd_2Cl_6$ Single Crystals: Synthesis, Nonlinear Optical Properties, and Stability, *Inorg. Chem.*, 2022, **61**, 8076–8082.

43 J. Cheng, Y. Deng, X. Dong, J. Li, L. Huang, H. Zeng, G. Zou and Z. Lin, Homochiral Hybrid Organic-Inorganic Cadmium Chlorides Directed by Enantiopure Amino Acids, *Inorg. Chem.*, 2022, **61**, 11032–11035.

44 W. Seo and K. M. Ok, Novel noncentrosymmetric polar coordination compounds derived from chiral histidine ligands, *Inorg. Chem. Front.*, 2021, **8**, 4536–4543.

45 H. Cheng, C. Cao, S. Teng, Z. Zhang, Y. Zhang, D. Wang, W. Yang and R. Xie, Sn(II)-doped one-dimensional hybrid metal halide [$C_5H_{14}NO$]$CdCl_3$ single crystals with broadband greenish-yellow light emission, *Dalton Trans.*, 2023, **52**, 1021–1029.

46 C. Shen, J. Liu, K. Wu, L. Xu, D. Sun, Y. Dang, J. Wang and D. Wang, High stability and moderate second-order nonlinear optical properties of hybrid lead-free perovskite [(CH_3)$_3NCH_2Cl$]$CdCl_3$ bulk crystals, *CrystEngComm*, 2023, **25**, 2264–2270.

47 W. Jin, W. Zhang, A. Tudi, L. Wang, X. Zhou, Z. Yang and S. Pan, Fluorine-Driven Enhancement of Birefringence in the Fluorooxosulfate: A Deep Evaluation from a Joint Experimental and Computational Study, *Adv. Sci.*, 2021, **8**, 2003594, DOI: 10.1002/advs.202003594.

48 Y. Liu, Y. Liu, Z. Lin, Y. Li, Q. Ding, X. Chen, L. Li, S. Zhao, M. Hong and J. Luo, Nonpolar Na10Cd(NO3)4(SO3S)4 Exhibits a Large Second-Harmonic Generation, *CCS Chem.*, 2021, 694–699, DOI: 10.31635/ccschem.021.202000758.

49 X. Hao, M. Luo, C. Lin, G. Peng, F. Xu and N. Ye, M(NH_2SO_3)$_2$ (M=Sr, Ba): Two Deep-Ultraviolet Transparent Sulfamates Exhibiting Strong Second Harmonic Generation Responses and Moderate Birefringence, *Angew. Chem., Int. Ed.*, 2021, **60**, 7621–7625.

50 H. Tian, C. Lin, X. Zhao, F. Xu, C. Wang, N. Ye and M. Luo, Ba(SO_3CH_3)$_2$: a Deep-Ultraviolet Transparent Crystal with Excellent Optical Nonlinearity Based on a New Polar Non-π-conjugated NLO Building Unit $SO_3CH_3^-$, *CCS Chem.*, 2023, 1–22, DOI: 10.31635/ccschem.022.202202582.

51 R. H. Blessing, An empirical correction for absorption anisotropy, *Acta Crystallogr., Sect. A: Found. Crystallogr.*, 1995, **51**, 33–38.

52 G. M. Sheldrick, Crystal structure refinement with SHELXL, *Acta Crystallogr., Sect. C: Struct. Chem.*, 2015, **71**, 3–8.

53 A. Spek, Single-crystal structure validation with the program PLATON, *J. Appl. Crystallogr.*, 2003, **36**, 7–13.

54 P. Kubelka and F. Munk, An article on optics of paint layers, *Z. Tech. Phys*, 1931, **12**, 259–274.

55 S. K. Kurtz and T. T. Perry, A Powder Technique for the Evaluation of Nonlinear Optical Materials, *J. Appl. Phys.*, 1968, **39**, 3798–3813.

56 M. D. Segall, P. J. D. Lindan, M. J. Probert, C. J. Pickard, P. J. Hasnip, S. J. Clark and M. C. Payne, First-principles simulation: ideas, illustrations and the CASTEP code, *J. Phys.: Condens.Matter*, 2002, **14**, 2717.

57 V. Milman, B. Winkler, J. A. White, C. J. Pickard, M. C. Payne, E. V. Akhmatskaya and R. H. Nobes, Electronic structure, properties, and phase stability of inorganic crystals: a pseudopotential plane-wave study, *J. Quantum Chem.*, 2000, **77**, 895–910.

58 J. P. Perdew, K. Burke and M. Ernzerhof, Generalized gradient approximation made simple, *Phys. Rev. Lett.*, 1996, **77**, 3865.

59 J. S. Lin, A. Qteish, M. C. Payne and V. Heine, Optimized and transferable nonlocal separable *ab initio* pseudopotentials, *Phys. Rev. B: Condens. Matter Mater. Phys.*, 1993, **47**, 4174.

60 J. Lin, M.-H. Lee, Z.-P. Liu, C. Chen and C. J. Pickard, Mechanism for linear and nonlinear optical effects in β-BaB_2O_4 crystals, *Phys. Rev. B: Condens. Matter Mater. Phys.*, 1999, **60**, 13380.

61 S. N. Rashkeev, W. R. Lambrecht and B. Segall, Efficient *ab initio* method for the calculation of frequency-dependent second-order optical response in semiconductors, *Phys. Rev. B: Condens. Matter Mater. Phys.*, 1998, **57**, 3905.

62 H. Tllili, S. Walha, S. Elleuch, B. Fares Ali and H. Naïli, Structural, vibrational, DFT and optical studies of a new non-centrosymmetric hybrid material ($C_4H_{12}N_2$)[$CoBr_4$], *J. Mol. Struct.*, 2018, **1152**, 303–310.

63 J.-H. Yu, Q. Hou, T.-G. Wang, X. Zhang and J.-Q. Xu, *Structure characterization of 1:1 adducts of metal(II) halides and piperazine*, Elsevier Inc., 2007, vol. 180, pp. 518–522.

64 X.-Y. Zhang, Z.-Q. Zhou, W.-X. Bao, H.-X. Tang, R.-B. Fu, Z.-J. Ma and X.-T. Wu, New lead-iodide formates with a strong second-harmonic generation response and suitable birefringence obtained by the substitution strategy, *Chem. Sci.*, 2023, **14**, 136–142.

65 C. Shen, D. Sun, Y. Dang, K. Wu, T. Xu, R. Hou, H. Chen, J. Wang and D. Wang, ($C_4H_{10}NO$)PbX_3 (X = Cl, Br): Design of Two Lead Halide Perovskite Crystals with Moderate Nonlinear Optical Properties, *Inorg. Chem.*, 2022, **61**, 16936–16943.

66 J.-M. Gong, T. Shao, P.-Z. Huang, C.-Y. Su, M. Chen, D.-W. Fu and H.-F. Lu, Reversible Phase Transition and Second-Harmonic Response Based on a Zero-Dimensional Organic–Inorganic Hybrid Compound, *J. Phys. Chem. C*, 2022, **126**, 15274–15279.

67 X. Han, P. Cheng, R. Shi, Y. Zheng, S. Qi, J. Xu and X. H. Bu, Linear optical afterglow and nonlinear optical harmonic generation from chiral tin(IV) halides: the role of lattice distortions, *Mater. Horiz.*, 2023, **10**, 1005–1011.

68 C. Yang, X. Liu, C. Teng, Q. Wu and F. Liang, Syntheses, structure and properties of a new series of organic-inorganic Hg-based halides: adjusting halogens resulted in huge performance mutations, *Dalton Trans.*, 2021, **50**, 7563–7570.

69 J.-L. Qi, J. Wu, Y. Guo, Z.-P. Xu, W. Liu and S.-P. Guo, Quasi-linear CuX_2 (X = Cl, Br) motif-built hybrid copper halides realizing encouraging nonlinear optical activities, *Inorg. Chem. Front.*, 2023, **10**, 3319–3325.

70 F.-F. Mao, C.-L. Hu, X. Xu, D. Yan, B.-P. Yang and J.-G. Mao, $Bi(IO_3)F_2$: The First Metal Iodate Fluoride with a Very Strong Second Harmonic Generation Effect, *Angew. Chem., Int. Ed.*, 2017, **56**, 2151–2155.